

Chapter 3

Elementary mechanisms of shear-induced contact area reduction

3.1 Introduction

Solid contacts of soft materials such as elastomers and human skin have revealed complex changes to the contact morphology when submitted to an additional shear loading. Not only is the overall real contact area significantly reduced [17, 78], but it also becomes increasingly anisotropic [63]; two effects that have not been satisfactorily explained yet. For both effects, smooth sphere/plane contacts have been shown to obey similar behaviour laws as rough contacts [17, 63]. It is therefore appealing to investigate anisotropic shear-induced area reduction in such simpler, single sphere/plane contacts between smooth solids.

Experimentally, elastomeric sphere/plane contacts are known to evolve from a circular area under pure normal load to a smaller, ellipse-like area in macroscopic sliding regime. In order to identify the underlying mechanisms responsible for such contact area evolution, Barquins and Courtel [79] and Barquins [80] monitored the shape of a straight line scratched on the polymer surface perpendicular to the direction of motion (“passing line” method), showing that the contact area shrinkage occurs by a peeling process; and also confirmed the existence of an adhesive zone, whereas partial slip takes place in an annular region adjacent to the edge of the contact area. Later, Waters and Guduru [49] performed a similar experiment to the “passing line” method; their results showed that there was no slip visible within the contact area while it remained symmetric, as the line appeared to remain straight inside the entire contact area. They

concluded that the contact area reduction under shearing is due to a peeling process rather than a slip propagation. Note that the difference in terms of loading conditions (normal loadings and shearing speed) in the above-mentioned studies may play a role in the observed discrepancies. It should be also noted that both findings, from Barquins and Courtel [79] and Barquins [80] and Waters and Guduru [49], are made only along the observation of the shape of a straight central line of the contact, and the presence of the scratched line can affect the mechanical behavior of the interface.

In this context and in order to take the first step toward the main objective of the thesis, this chapter presents an experimental analysis of an elastomer/glass interface, similar to those of Sahli et al. [17, 63], to identify the elementary mechanisms responsible for contact area reduction and their relative contributions. The strategy is based on the incorporation of particles at the proximity of the elastomer surface and on their use as local tracers for the motion of the entire frictional interface during incipient tangential loading under several constant normal loads. The relevance of the detected mechanisms will be compared with a non-adhesive model that shows a quantitative agreement with recent large-load experiments, with no adjustable parameter.

3.2 Experimental procedure

3.2.1 Tangential loading experiments

The custom-built setup presented in Section 2.2.1 was used to shear the interface between a smooth glass plate and a cross-linked PDMS sample (nearly incompressible, $E = 1.5 \pm 0.1$ MPa) with a spherical cap seeded with a layer of particles about $16\ \mu\text{m}$ below the surface (see details in Section 2.1.2, sample of the type S1R9P). The experiments were performed in a normal sample attachment configuration, as illustrated in Fig. 2.5, under 4 different constant normal loads, $P = 1.85\ \text{N}$, $0.54\ \text{N}$, $0.25\ \text{N}$, and $0.05\ \text{N}$. Respectively, $21\ \text{s}$, $14\ \text{s}$, $13\ \text{s}$, and $22\ \text{s}$, after the contact has been created for each experiment, a constant driving velocity $V = 0.1\ \text{mm/s}$ was imposed on the glass plate, over a total distance of $2\ \text{mm}$. Images of the interface were acquired during the glass displacement with a lateral square pixel of $7.7\ \mu\text{m}$ for $P = 1.85\ \text{N}$, and $9.0\ \mu\text{m}$ for the others normal loads, in the contact plane. See section 2.2.2 for more specifications and a detailed description of the experiment.

The evolution of the tangential force Q as a function of the imposed displacement d of the glass plate for the different normal loads is shown in Fig. 3.1 (solid black line, left axis). The incipient tangential loading of the interface reaches a maximum, denoted as the static friction force Q_s (at displacement d_s), before a full sliding regime during which $Q < Q_s$.

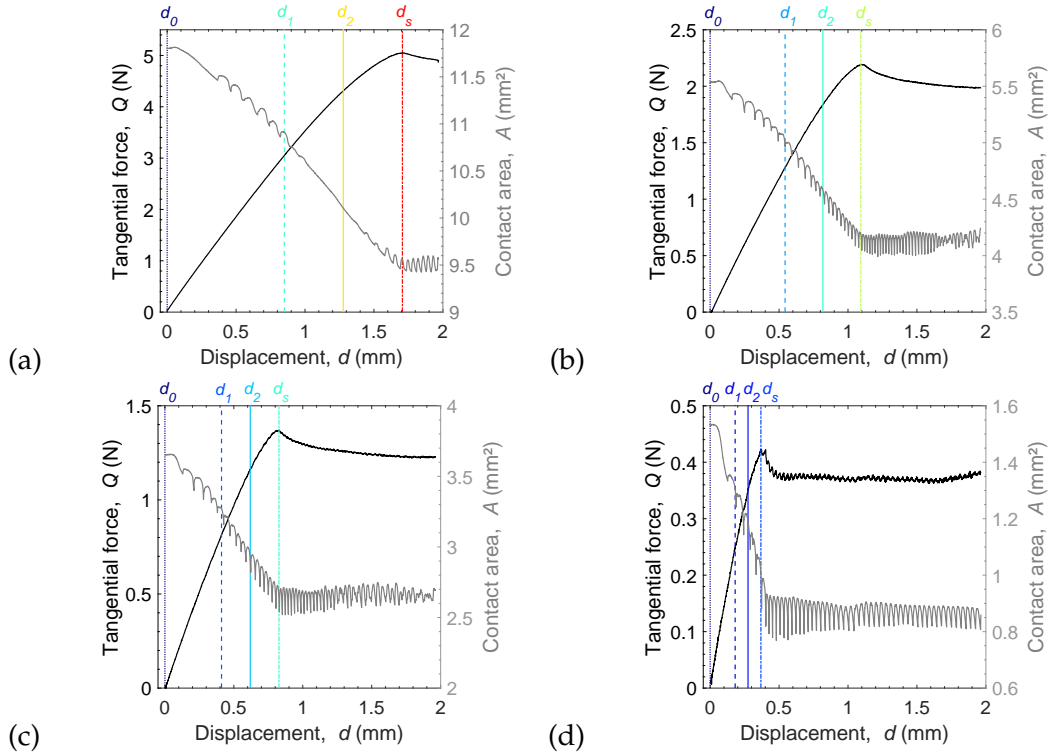


Figure 3.1: Evolution of the tangential force Q (solid black line, left axis) and of the contact area A (solid grey line, right axis) as a function of the imposed displacement d of the glass substrate. Four displacement values are indicated, which will be used in further figures. The static friction force Q_s occurs at displacement d_s . $V = 0.1 \text{ mm/s}$. (a) $P = 1.85 \text{ N}$, (b) $P = 0.54 \text{ N}$, (c) $P = 0.25 \text{ N}$, and (d) $P = 0.05 \text{ N}$.

The incorporation of particles into the proximity of the PDMS sphere surface is the strategy that allows us to observe any local phenomenon occurring within the contact area during tangential loading. However, in order to carry out such observation, some specifications are required: (i) the particles must be visible by the camera regarding their sizes and light reflection ability, providing high contrast in the contact area; (ii) they must be located close to the sphere surface, but not on the very surface to avoid affecting the mechanical response of the interface; (iii) the layer of particles thickness must be thin to avoid differential displacement due to different depths; (iv) the particles in the layer must be well scattered and sufficiently isolated from one another to be monitored individually by a PIV (Particle Image Velocimetry) type procedure.

Among several tested particles candidates (*e.g.*, aluminum oxide, boron carbide, and glass micro-spheres), silver particles were the ones that best satisfied these requirements, however they have random shapes with a mean area of $9.2 \times 10^2 \mu\text{m}^2$ (ranging from $2.9 \times 10^2 \mu\text{m}^2$ to $67.1 \times 10^2 \mu\text{m}^2$).

Typical raw images of the contact interface, for the four normal loads, are shown in Fig. 3.2(a–d) for four different displacements (shown in Fig. 3.1): d_0 before any shear, d_s the displacement at the static friction peak Q_s , and d_1 and d_2 two intermediate displacements. Full movies are available, as supplementary material, in Appendix A, as Movies M185, M054, M025, and M005 for $P = 1.85 \text{ N}$, 0.54 N , 0.25 N , and 0.05 N , respectively. The contact region corresponds to the biggest region of dark pixels. In all subsequent figures, the leading (resp. trailing) edge is always on the left (resp. right) side. As mentioned in the description of the optical acquisition system in Chapter 2, the contact regions are not uniformly dark, but are sprinkled with random bright spots that are due to light reflection on the particles incorporated close to the elastomer surface. The upper right dark region is a marker drawn on the glass substrate to monitor its macroscopic motion.

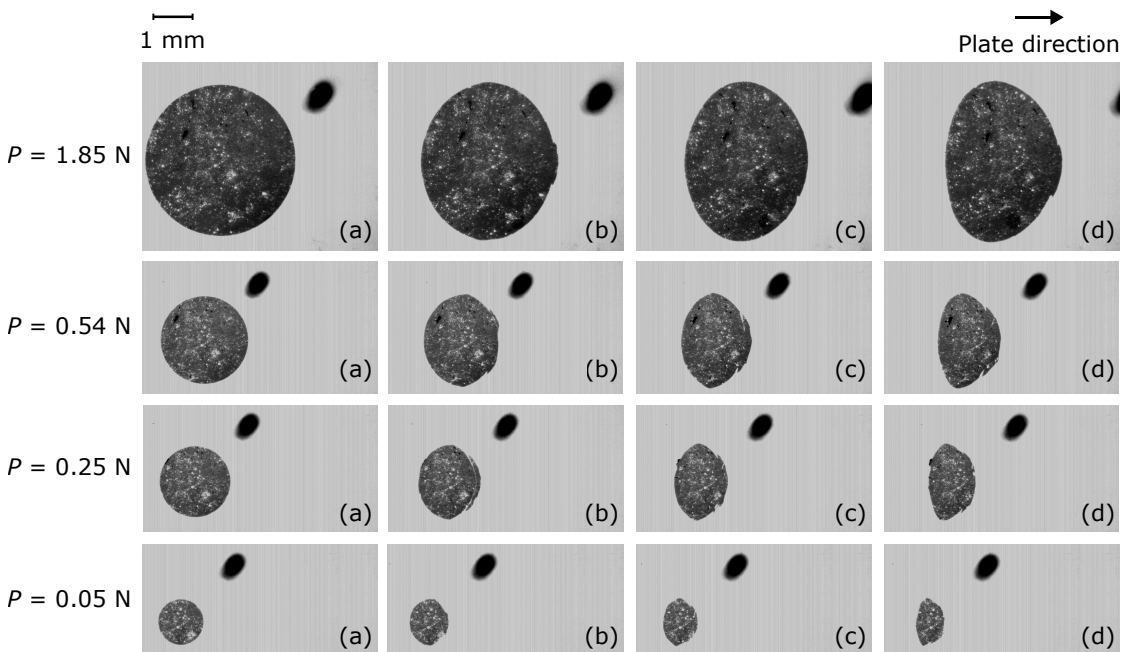


Figure 3.2: Raw images of the contact interface at the four displacements shown in Fig. 3.1. (a): d_0 , (b): d_1 , (c): d_2 , and (d): d_s , for the four normal loads, 1.85 N , 0.54 N , 0.25 N , and 0.05 N . The main dark region is the contact area, bright spots are the particles, and the upper right dark region is a marker drawn on the glass substrate to monitor its macroscopic motion. The images are in the frame of the camera and the leading edge is on the left side.

Figures 3.3(a-d) show typical contours of the contact, the inner area of which defines the contact area A . The evolution of A as a function of the imposed displacement of the glass plate is shown in Fig. 3.1 (grey lines). For all experiments, both, Q and A curves, in Fig. 3.1 present the same qualitative behavior as previous experiments in the literature [17, 49, 55], which shows that the insertion of particles into elastomer spheres does not significantly affect the mechanical response of the interface. The oscillations observable in the $A(d)$ curves in Fig. 3.1 originate from so-called detachment folds [80] occurring at the trailing edge of the contact.

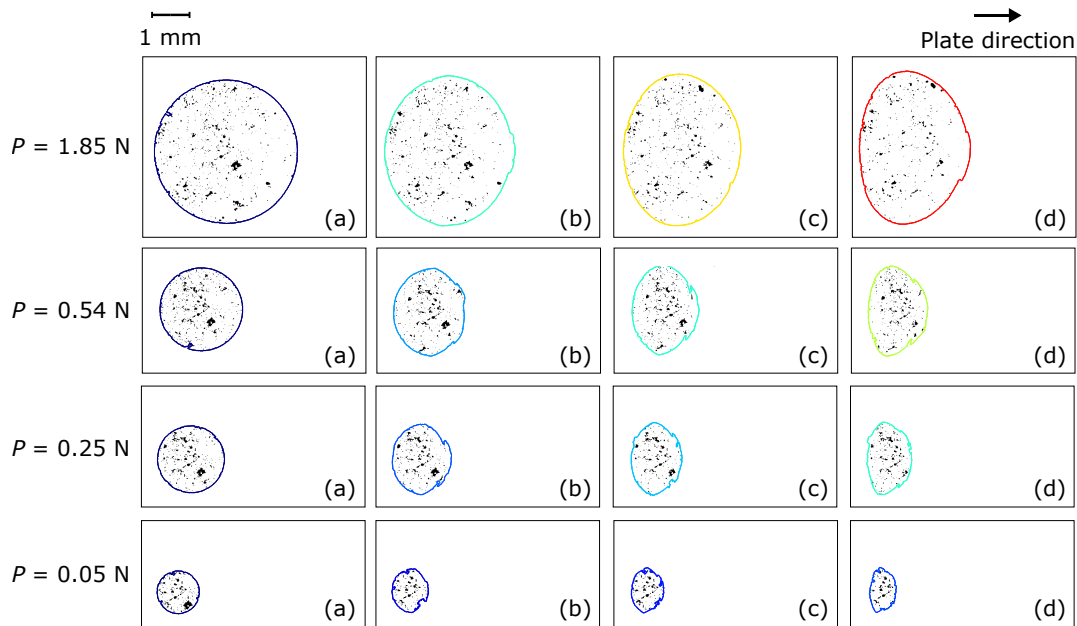


Figure 3.3: Segmented images from raw images of Fig. 3.2 at the four displacements (a): d_0 , (b): d_1 , (c): d_2 , and (d): d_s , for the four normal loads, 1.85 N, 0.54 N, 0.25 N, and 0.05 N. In (a-d) of each experiment, the contours are those of the contact (same colors as in Fig. 3.1), the inner area of which defines the contact area; black spots correspond to the particles. The images are in the frame of the moving glass plate. The leading edge is on the left side.

3.2.2 Image processing: segmentation and particle tracking

The bright spots present in the images of Fig. 3.2 were used as tracers of the contact evolution by applying a homemade tracking procedure detailed hereafter. The main aim of this tracking code is to generate a data set in which the x - and y -positions of each tracer are given for each image/time-step. Note that only the tracers at the vertical of the contact regions are visible.

Image analysis followed the operations described in Section 2.3.1 and after the segmentation process, where basically the raw images are classified into in- and out-of-contact pixels, a noise reduction process was performed on all images. In this denoising process, all objects (set of connected pixels) with an area of a single pixel are removed by successively performing two morphological operations, erosion and dilation, with a 3×3 square structuring element (set of coordinate points whose width is 3 pixels). Then the closest remaining objects are connected by successively performing the two same operations in reverse order, *i.e.* dilation and erosion. This results in connecting all the objects within a distance of less than $23 \mu\text{m}$ for $P = 1.85 \text{ N}$ and less than $27 \mu\text{m}$ for the other normal loads. In such operations, the center pixel of the structuring element, called the origin, is aligned with each pixel in the image that has a value of 1 (white) and each pixel of the structuring element is included (resp. excluded) in the dilated (resp. eroded) image. Those binary images were then used as inputs to the tracking code.

The tracking processing, as described in Algorithm 1, identifies, only on the initial image, objects whose area is strictly larger than 4 pixels. Those objects are then considered as tracers of the contact evolution for upcoming analysis. For each tracer, the centroid (C_x and C_y) and the x - and y -widths of the smallest rectangle enclosing it (W_x and W_y) are stored. Next, the trajectory of each tracer is found by searching for its successive positions on all images. For two successive images, the following procedure is applied to each tracer:

- extracts two sub-images from both successive images (at steps i and $i+1$): their common extraction positions correspond to the position, $C_x(i)$ and $C_y(i)$, of the tracer and their widths correspond to $W_x(i)$ and $W_y(i)$ increased by 5 pixels on all four sides to account for the dilation operation performed on the next process. This sub-image procedure is implemented to improve computing performance by significantly increasing the image processing speed in MATLAB® (The MathWorks, Inc.).
- performs a dilation operation with a 3×3 square structuring element only on the sub-image at step i . This dilation enlarges the boundaries of the tracer by a larger

amount than the expected theoretical travel distance (Δd_{\max}) of the slider between two successive images in the steady sliding regime, $\Delta d_{\max} = 1 \mu\text{m} \sim 0.14 \text{ pixel}$.

- multiplies pixel by pixel the two resulting sub-images, *i.e.* the dilated one at step i with the unmodified one at step $i+1$.
- finds all objects in the image resulting from the multiplication and stores the position of the object as the coordinates, $C_x(i+1)$ and $C_y(i+1)$, of its center of mass in the full image. If multiple objects are detected, only the closest object to the center of the sub-image at step i is considered. If there is no object, then the trajectory ends.

Therefore, the outcome of the tracking process is a data set in which the centroid position, $C_x(i)$ and $C_y(i)$, of each tracer is given in the laboratory frame, for all image, *i.e.* for each time step. Then, all tracers containing non-realistic trajectory changes (greater than 3 pixels, that is, greater than $23 \mu\text{m}$ for $P = 1.85 \text{ N}$ and $27 \mu\text{m}$ for the other normal loads) in the position of the tracer between two consecutive images were removed. Finally, the displacement of the glass plate was subtracted from all trajectories (for instructions on glass displacement extraction, refer to Section 2.3.1). In other words, we place the trajectories in the frame of the glass substrate.

3.3 Results and analysis

In this section, based on the results of the particle tracking procedure, a thorough analysis of the tracers' behavior (appearance/disappearance and relative motion with respect to their initial position and adjacent tracers) is conducted. First, the existence of elementary mechanisms of contact area evolution on the onset of the macroscopic sliding is searched. Second, the evolution of the tracers displacement throughout the entire experiment is investigated.

3.3.1 Elementary mechanisms of contact area evolution

As mentioned in Section 3.2.1, the particles are only visible in the vertical direction of the contact area, which provides the possibility to investigate the existence of elementary mechanisms responsible for the contact area evolution.

Algorithm 1: Particles tracking code

Input: Segmented images**Output:** Data set of tracer trajectories

```

1 begin
2   detection of the number of objects in the first image;
3   define as tracer all objects whose area > 4 pixels;
4   store the position of all tracers as the coordinates ( $C_x(i)$  and  $C_y(i)$ ) of its
      centroid;
5   store x- and y-widths ( $W_x(i)$  and  $W_y(i)$ ) of the smallest rectangle enclosing
      each tracer.
6   for images do
7     take two successive images at steps  $i$  and  $i+1$ .
8     for tracers do
9       extract two sub-images from the couple successive images at  $i$  and
           $i+1$ : their common extraction coordinates correspond to the
          position,  $C_x(i)$  and  $C_y(i)$ , of the tracer and their widths correspond
          to  $W_x(i)$  and  $W_y(i)$  increased by 5 pixels on all sides to account for
          the dilation operation that is performed on the next process.
10    perform a dilation operation with a 3x3 square structuring element
        only on the sub-image at step  $i$ 
11    multiply pixel by pixel the sub-image (dilated) at step  $i$  and the
        sub-image (unmodified) at step  $i+1$ 
12    find the number of objects (connected pixels) in the image resulting
        from the multiplication
13    if  $object = 1$  then
14      save tracers as coordinates ( $C_x(i + 1)$  and  $C_y(i + 1)$ ) of its centroid
          in the full image.
15    else if  $object > 1$  then
16      only the closest object to the center of the sub-image at step  $i$  is
          considered.
17    else
18      tracer trajectory ends.
```

Tracers that were initially in contact and no longer exist at the onset of the macroscopic sliding (at Q_s), means that they have been lifted out-of-contact. This first elementary mechanism of area variation is then named “contact lifting” (or simply “lifting”). On the contrary, tracers that were initially out-of-contact, but came into contact during the incipient loading phase demonstrate the second elementary mechanism of area variation, that is named “contact laying” (or “laying”). Finally, the third elementary mechanism is related to inhomogeneous slip and in-plane deformation within the contact zone and leads to either “in-plane compression” or “in-plane dilation”.

In an attempt to quantify those mechanisms we make use of two graphical approaches: Voronoi tessellation and Delaunay triangulation. In an overview definition, Voronoi tessellation of a finite set of unique sites is a collection of regions, called cells, that divide up an Euclidean space. Each cell corresponds to one of the sites, and all the points in one region are closer to the corresponding site than to any other site [81]. Its dual graph is a Delaunay triangulation, where two sites are connected by an edge in the Delaunay triangulation if they belong to adjacent Voronoi cells. Delaunay triangulation is formed by a net of triangles satisfying the empty circumcircle criterion: the circumcircle of each triangle contains only the vertices of the triangle, and there are no site of other triangles inside the circumcircle. Delaunay triangulations also maximize the minimum angle of all triangles in the triangulation [81, 82]. Figure 3.4 illustrates an example of a Voronoi diagram (solid black lines) and its dual Delaunay tessellation (dashed red lines) for a set of 11 sites (open black disks).

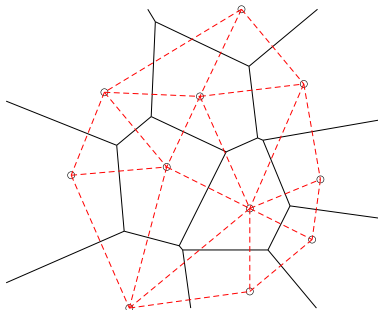


Figure 3.4: A Voronoi diagram (solid black lines) and its dual Delaunay tessellation (dashed red lines) for a set of 11 sites (open black disks).

Contact lifting

The feature of local contact lifting is that a tracer disappears from the image when it is reached by a moving contact periphery, which means that a point of the elastomer initially in contact with the glass has been lifted out-of-contact. Such criterion of being close to the contact edge is used to distinguish tracers that are truly lifted from tracers that disappear due to noise in the images and tracking procedure.

In practice, we look for the tracer's trajectory which ends at a position less than 20 pixels from the contact edge (*i.e.* $154 \mu\text{m}$ for $P = 1.85 \text{ N}$, and $180 \mu\text{m}$ for the others normal loads). All these tracers are represented as disks in Fig. 3.5. Filled disks correspond to the position of the lifted tracers in the initial image (at d_0), and open disks indicate the position when the tracers disappear.

It appears that a considerable amount of tracers are indeed lifted during the incipient tangential loading of the contact for all normal loads. The majority of them are located at the trailing edge of the contact (on the right side), where points of the glass are continuously driven out of the contact region. Some of them are located at the leading edge of the contact, but may be tracers that were initially close to the contact edge and disappeared due to tracking noise. However, for the smallest normal load, 0.05 N , shown in Fig. 3.5(d), it seems that a real lifting also occurs at the contact leading edge since the contour on the left side moves inward the contact area.

The color of each disk in Fig. 3.5 corresponds to the glass displacement at which the tracer disappears. It seems that the colors of the filled disks are spatially organized, from blue (early disappearance) for the rightmost disks to red (late disappearance) for the leftmost disks. Such a pattern indicates that lifting occurs through an inward front propagation, starting from the trailing edge of the contact (and also from the leading edge for the small load, $P = 0.05 \text{ N}$, see Fig. 3.5(d)).

In order to quantify the contact area lost due to lifting, we assign a representative individual area to each tracer. To this end, we performed a bounded Voronoi tessellation of the centroid of the tracers in the initial image, the boundary being the contact contour. Each tracer was thus assigned the area of its Voronoi cell. In Fig. 3.5, the grey cells correspond to all Voronoi cells assigned to lifting in the final image (at d_s). Then, for each image, the lifted area is calculated as the sum of the Voronoi cells area of all

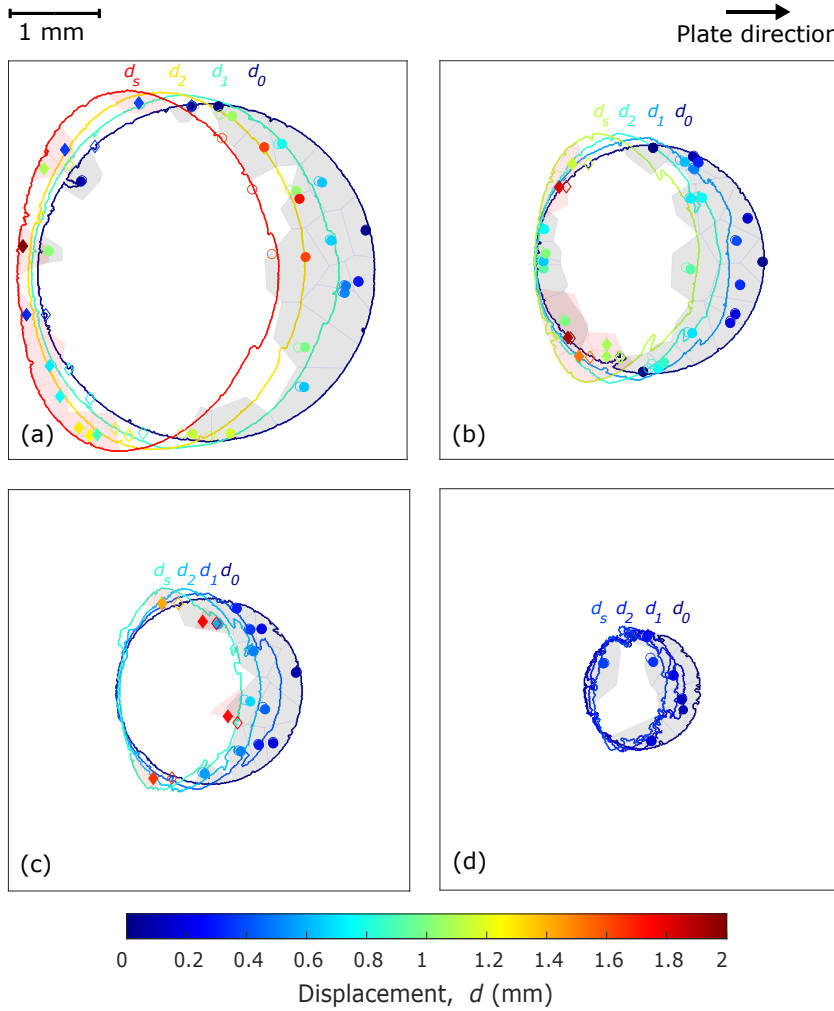


Figure 3.5: Measurement of the lifted and laid areas. (a) $P = 1.85 \text{ N}$, (b) $P = 0.54 \text{ N}$, (c) $P = 0.25 \text{ N}$, and (d) $P = 0.05 \text{ N}$. Solid colored lines: contours of the contact at the four selected displacements (same colors as in Figs. 3.1, 3.3, and 3.9). The contours are in the frame of the moving glass plate. The leading edge is on the left side. Open (resp. filled) disks: position of the lifted particles when they disappear (resp. at d_0). The symbol color corresponds to the displacement at which the particle is lifted (same color code as for the contours). Grey cells: cells of the Voronoi tessellation at d_0 associated to lifted particles at d_s . Filled (resp. open) diamonds: position of the laid particles at d_s (resp. when they appear). The symbol color corresponds to the displacement at which the particle are laid. Red cells: cells of the Voronoi tessellation at d_s associated to laid particles at d_s .

lifted tracers so far. The evolution of the lifted area along the experiments is shown in blue in Fig. 3.6 and is stair-like because each lifting event abruptly increases the lifted area by a finite amount (a cell area). The estimated final lifted area for each normal load is shown in Table 3.1. It can be seen that the contact area reduction increases with the decrease of the normal load, from $\sim 19\%$ to $\sim 35\%$; one expects the lifted area to behave in the same way. However, the values of lifted cells presented on Table 3.1 must be carefully observed, since, for $P = 1.85 \text{ N}$ (Fig. 3.5(a)) and $P = 0.54 \text{ N}$ (Fig. 3.5(b)), it

is taking into account the lifted cells, on the leading edge (left side), presumably associated to a noise in the images and not to a real contact lifting. This misattribution leads to an overestimation of the lifted area of $\sim 2\%$ and $\sim 7\%$, respectively.

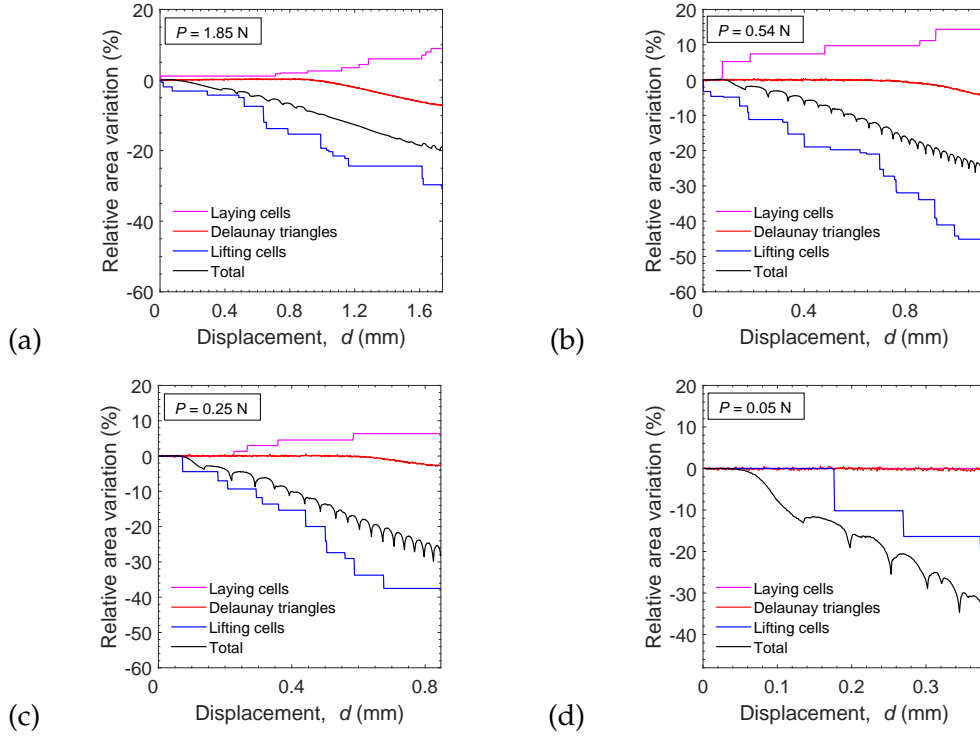


Figure 3.6: Contributions of the various mechanisms to the area variation. (a) $P = 1.85 \text{ N}$, (b) $P = 0.54 \text{ N}$, (c) $P = 0.25 \text{ N}$, and (d) $P = 0.05 \text{ N}$. Relative area variation, $\Delta A / A_0$, vs the imposed displacement, d . Black: reduction of the total contact area. Blue (resp. magenta): area lost (resp. gained) by lifting (resp. laying), measured as in Fig. 3.5. Red: area variations due to slip-induced in-plane deformation, measured as in Fig. 3.7.

Table 3.1: Estimated contribution of contact area reduction mechanisms.

P	Area reduction	Lifted cells	Laid cells	Delaunay triangles
1.85 N	$\sim 19\%$	$\sim 31\%$	$\sim 9\%$	$\sim 7\%$
0.54 N	$\sim 24\%$	$\sim 45\%$	$\sim 14\%$	$\sim 4\%$
0.25 N	$\sim 28\%$	$\sim 38\%$	$\sim 6\%$	$\sim 3\%$
0.05 N	$\sim 35\%$	$\sim 46\%$	0 %	< 1 %

Contact laying

The mechanism of laying, *i.e.* points of the elastomer getting into contact with the glass plate upon shearing, can be analyzed similarly to lifting. The same analysis as in the previous section is performed here, but backward in time: the first image considered is the one at the static friction peak (at d_s), while the last one is the initial image (at d_0).

In doing so, tracers appearing close to the contact periphery in forward time are the ones disappearing in backward time and therefore those detected by our reverse procedure.

Figure 3.5 shows the results of this analysis, where the locations of the laid tracers are shown in the final configuration (at d_s , filled diamonds) or where they appear (open diamonds). Laid tracers are found at the leading edge of the contact, beyond the initial contact region. Only for $P = 0.25\text{ N}$ (see Fig. 3.5(c)), there are two laid tracers found at the trailing edge of the contact (right side), but as mentioned in the lifting analysis, these tracers may initially be located at the proximity of the contact edge and disappeared in backward time due to noise in the images. The filled diamonds color, evolving from blue to red, corresponds to the position at which they appear and is again spatially organized, indicating that contact laying occurs through an outward front propagation starting at the leading edge of the contact. No laid tracer is found for $P = 0.05\text{ N}$ (Fig. 3.5(d)), indicating that laying mechanism may not occur under such small normal load, a regime in which adhesion stresses are expected to dominate [49]. However, the very low resolution of our analysis in such a small contact area with very few tracers does not fully validate this hypothesis and further investigations are required.

The amount of contact area gained via laying is estimated using a bounded Voronoi tessellation performed in the final contact configuration (at d_s). In Fig. 3.5, the red cells correspond to the area assigned to laying in the final image (at d_s). At each instant, the laid area is counted as the sum of the areas of all laid tracers. The evolution of the area gained due to laying is shown in magenta in Fig. 3.6. Unlike lifting, the laying mechanism initiates only after a finite shear is applied, and it seems to increase as the normal load increases, as shown in Table 3.1. The values of laid cells consider the ones attributed to noise in the images in $P = 0.25\text{ N}$ (Fig. 3.5(c)) with tracers located at the trailing edge of the contact and in $P = 0.54\text{ N}$ (Fig. 3.5(b)) with tracers located inside the initial contour at the leading edge, resulting in an overestimation of the laid areas of $\sim 3\%$ for both $P = 0.54\text{ N}$ and $P = 0.25\text{ N}$.

In-plane deformation

In previous analyses of tracers' displacement, it is observed that a peripheral slip region gradually invades the contact replacing a central stuck area as shear increases. Moreover, in both contact lifting and laying, the filled and open markers have different

locations regarding the glass plate (see Fig. 3.5), which clearly means that slip occurs between the two instants. Local lifting is preceded by a slip, while local laying is followed by a slip. In both analysis, slip is found to be roughly parallel, but opposed to the glass plate motion, and occurs in both the leading and trailing regions of the contact.

From the combination of backward slip at the trailing edge and a stuck zone at the contact center, one expects in-plane compression of the elastomer in the trailing half of the contact. Symmetrically, in-plane dilation is expected in the leading half. The overall effect of both types of in-plane deformation must lead to a change in contact area that was estimated as follows.

Only the tracers present in the initial image and that could be followed from d_0 to d_s , thus excluding the lifted and laid ones, were considered. A Delaunay triangulation was performed to mesh these tracers in the initial image, as shown as a grey network in Fig. 3.7(a). As shear increases, the tracers move relative to each other. By keeping the same connectivity within the mesh, but updating the position of the tracers (sites), the relative changes of the areas of all the triangles of the initial Delaunay triangulation were monitored and the local in-plane deformation is thus estimated as these relative area changes.

Figure 3.7 shows, for the four normal loads (in the rows), the evolution of the in-plane deformation field as shear increases (cold colors for compression, warm ones for dilation). Before d_1 (b) no deformation is observed, presumably because the slip front has not reached yet the fraction of initial contact covered by the Delaunay triangulation. Between d_1 (b) and d_2 (c), a compressed region sets in at the trailing side of the contact; the absence of a detectable symmetrical dilated region on the leading side suggests that the propagation of the slip front is not axisymmetrical, as usually considered in models of the incipient shear loading of circular linear-elastic contacts [83]. At d_s (d), a heterogeneous slip-induced in-plane deformation field is fully developed, with a large compression region on the trailing side and a smaller dilation region on the leading one. Those field measurements are qualitatively consistent with previous measurements of Barquins and Courtel [79] and Barquins [80] on a similar system, but made only along the central line of the contact in steady-state sliding.

The evolution under shear of the sum of the total area contained in the deforming

Delaunay triangulation is shown in red in Fig. 3.6. This area remains essentially unchanged during the first half of the experiment, and then progressively decreases by up to about 7 %, 4 %, 3 %, and <1 % of the initial contact area for $P = 1.85 \text{ N}$, 0.54 N , 0.25 N , and 0.05 N , respectively.

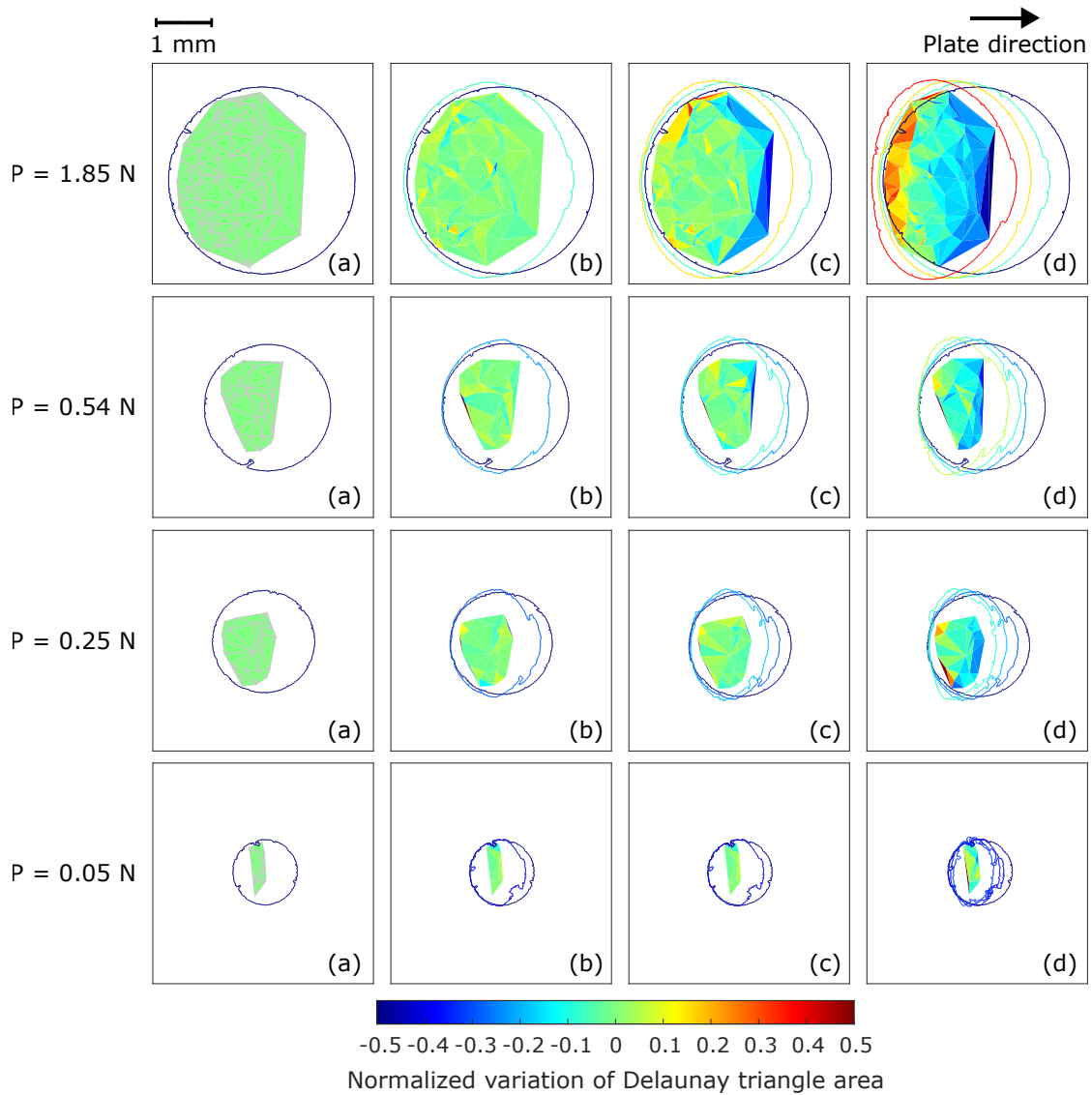


Figure 3.7: In-plane deformation measurement. (a) Grey network: Delaunay tessellation based on all tracers of the first image (at d_0) that can be tracked until d_s . (b-d) Snapshots of the evolution of the Delaunay triangles (defined at d_0) at successive instants: d_1 (b), d_2 (c), and d_s (d). Solid lines are the contours of the contact at d_0 , d_1 , d_2 , and d_s with the same color code as in Figs. 3.1, 3.3 and 3.5. The color of each triangle corresponds to its relative area change with respect to the situation at d_0 (see colorbar). Colder (resp. warmer) colors mean in-plane compression (resp. dilation).

Uncertainties on the area changes evaluation

The uncertainties of the above experimental measurements are mainly related to the finite surface density of useful tracers. Table 3.2 shows the number of tracers larger than 4 pixels in the initial image of each experiment, on which the tracking procedure has been applied. As well as the amount of tracers useful for the Voronoi (*i.e.* corresponding either to lifted or laid tracers) and Delaunay analysis. Not all the tracers were used in the analyses due to the exclusion of the tracers containing non-realistic trajectories, see 3.2.2.

Table 3.2: Number of tracers applied on the analyses.

P	Tracers	Voronoi analysis	Delaunay analysis	Excluded
1.85 N	263	31	174	100
0.54 N	140	30	48	81
0.25 N	89	16	34	52
0.05 N	48	7	12	27

Table 3.3 summarizes the average Voronoi area of the useful cells and their fraction of the initial contact area. In practice, due to the randomness of the tracers' location, the individual areas varied considerably, as shown in the fourth column. Because the Voronoi cells are the smallest units of area involved in the lifting (resp. laying) analysis, the evolution rate of the estimated lifting (resp.laying) area suffers from large fluctuations. In fact, each drop (resp. rise) in the blue (resp.magenta) curves of Fig. 3.6 are linked to the simultaneous subtraction (resp.addition) of one or more Voronoi cells with a random area.

Table 3.3: Voronoi areas.

P	Avg. Voronoi area (mm^2)	Avg. Voronoi area (%)	Range of Voronoi area (%)
1.85 N	0.15	1.33	0.21 - 3.99
0.54 N	0.12	2.20	0.21 - 5.27
0.25 N	0.10	2.74	1.66 - 4.71
0.05 N	0.10	6.76	3.55 - 9.86

Avg: average

In addition, the final estimate of the lifted area is actually an overestimation. Because, for the latest lifted cells, the fraction of area at the left of the tracer has not been really lifted yet. The same discussion applies to the estimation of the final laid area. Both effects would be reduced with a larger density of tracers, resulting in smoother curves with smaller step amplitudes.

Concerning the estimate of in-plane deformation, the region probed by the Delaunay-based analysis is only a fraction of the target region (the part of the initial contact that never lifts nor lays during the experiment). This is apparent for instance on Fig. 3.7(a), for all normal loads, with the white strip between the leading part of the contact contour and the Delaunay triangulation. An analogous strip is also lost on the trailing side, between the Delaunay triangulation and the lifted region. Those strips are due to the fact that only the tracers that could be followed from d_0 to d_s (excluding the lifted and laid ones) were considered in this analysis. Because the largest strains are precisely expected to be found on the periphery of the Delaunay triangulation (see Fig. 3.7(d)), the estimate of the area lost by in-plane deformation may be subject to a significant error. The values in Table 3.1 of area reduction due to this mechanism must then be taken with caution.

3.3.2 Evolution of tracers displacement

The displacement of each tracer relative to its initial position in the contact area Δd_t is measured and show in Fig. 3.8 as a function of the time t for the four normal loads. The instant of the static friction force Q_s is indicated as a vertical line. The trajectory of tracers considered to be lifted out-of-contact (see Section 3.3.1) before the end of the experiment are shown in black, while colored lines represent the tracers present from the initial (at $t = 0$ s) to the end of the experiment (at $t = 20$ s). Cold colors are for the smallest displacements and warm colors for the largest ones at Q_s .

We can see in Fig. 3.8 that each particle, basically, has two main regimes. The first one, at a low times/tangential displacements, corresponds to a stuck regime during which the particles stay nearly at the same position in the glass moving frame, which means that they are stuck to the moving glass plate. In reality, one can notice that in this regime, especially for the highest loads, the position of each particle does not remain exactly unchanged (vanishing displacement). This small unexpected displacement can presumably be attributed to the bulk deformation of the PDMS under shear. Indeed, the particles are not precisely located at the interface ($\sim 16 \mu\text{m}$ in depth) and thus they can be slightly displaced in the direction of the shear even if no relative displacement (slip) occurs at the interface. Note that a similar phenomenon was observed at a rough contact interface in [62]. The second regime, at large times/tangential displacements,

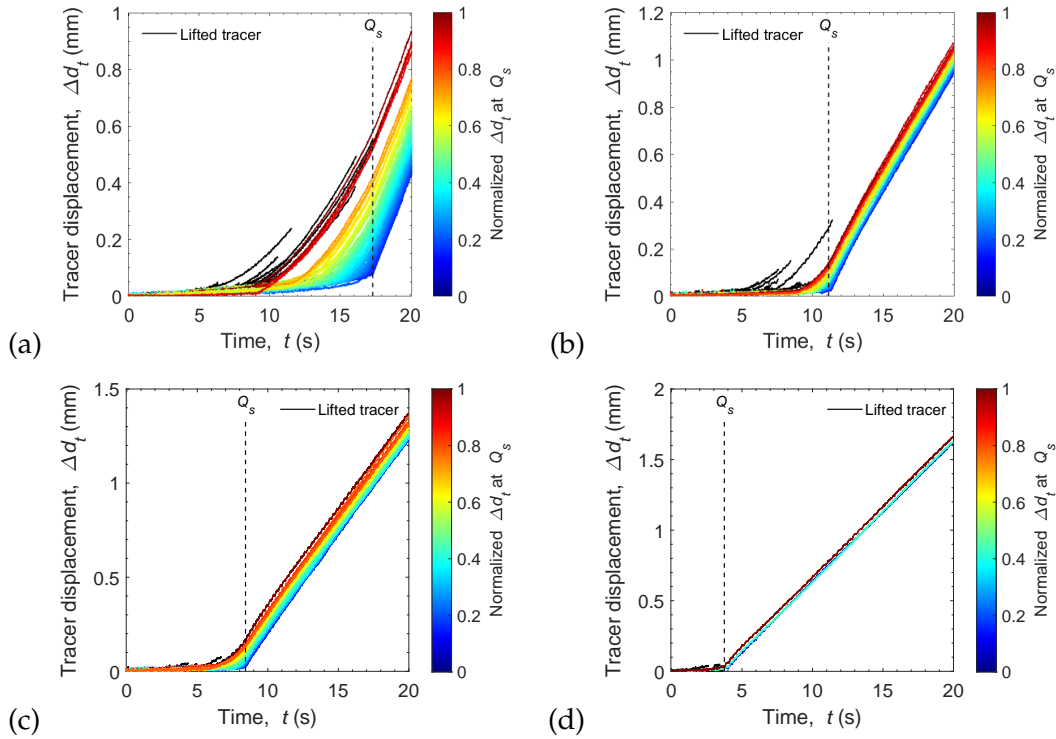


Figure 3.8: Tracers displacement *vs* time. (a) $P = 1.85$ N, (b) $P = 0.54$ N, (c) $P = 0.25$ N, and (d) $P = 0.05$ N. Vertical line indicates the instant of the static friction force Q_s . Black lines: tracers' trajectories that are lifted out-of-contact before the end of the experiment (at $t = 20$ s). Colored lines: tracers present from the beginning to the end of the experiment. Cold colors are for the smallest displacements and warm colors for the largest displacements at Q_s .

corresponds to a full sliding regime during which the particles stay in place in the laboratory frame, *i.e.* move at the glass velocity in the glass frame.

By focusing on the transitions between those two regimes, for each particle, three important observations can be made: (i) the transitions at the various tracers are spread over a period of approximately half the duration to reach the peak; (ii) the order of departure of the transition respects the color code used which means that the first particles that have slipped (warm color) are those in the end which have slipped the most; and, (iii) the larger the time/displacement at which the transition occurs, the more abrupt it is: the last particle which slips (*i.e.* the one corresponding to the darkest blue curve) clearly shows a sharp kink between the two regimes.

All of these observations seem to indicate that there is a temporal and spatial organization in the transition to sliding within the interface. Then, to better spatially address each tracer displacement in the contact area, their magnitude is represented by iso-displacement contours in Fig. 3.9.

As in Fig. 3.8, cold colors are for the smallest displacements and warm colors for the

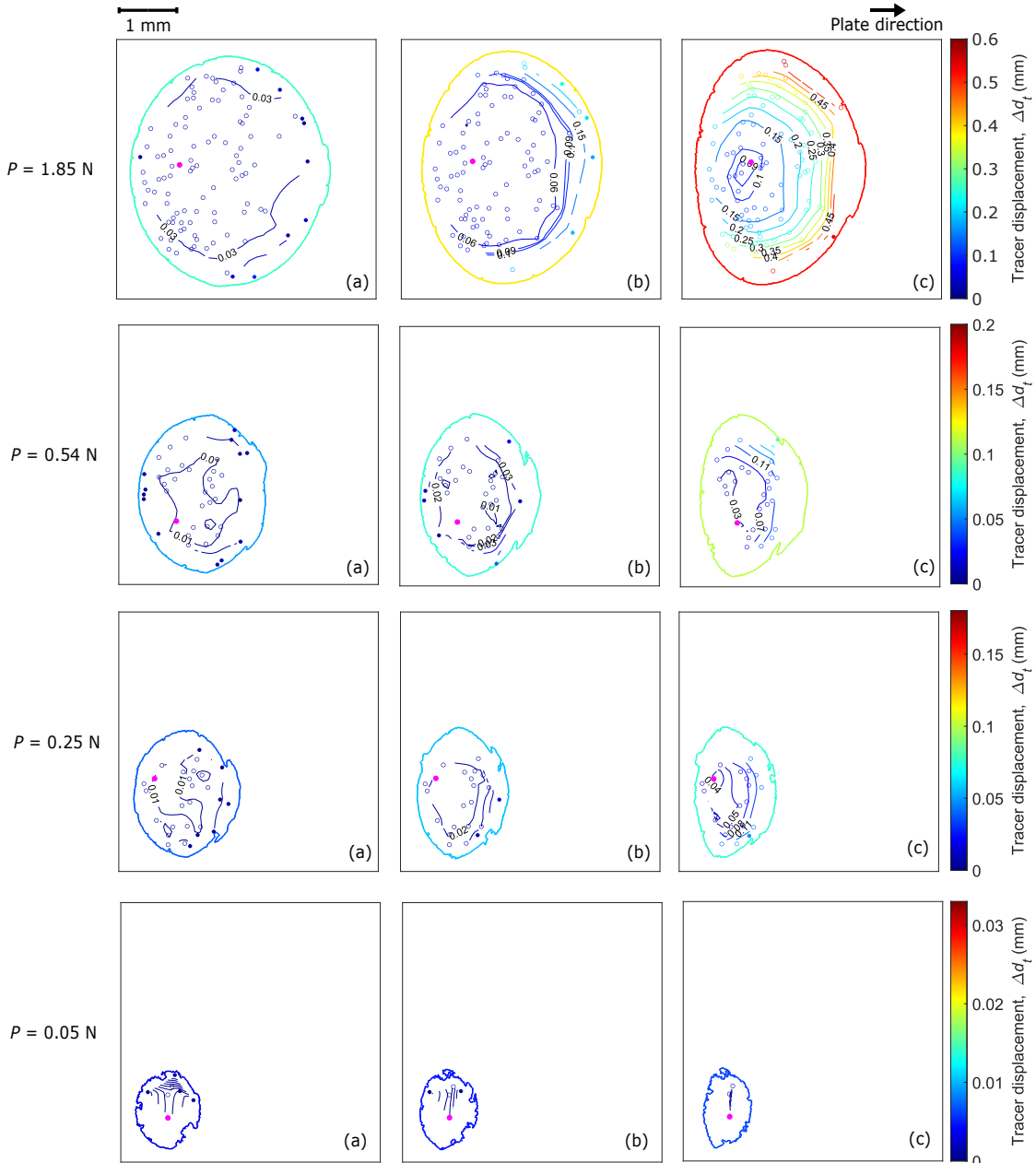


Figure 3.9: Iso-displacement contours of the tracers displacement for all normal loads. The outer contour defines the contact area at the instants (a) d_1 , (b) d_2 , and (c) d_s with the same color code as in the previous Figs. 3.1 and 3.3. Lifted tracers at Q_s , i.e. tracers that up to Q_s will be lifted, are represented as filled disks (\bullet), while open disks (\circ) are for tracers present throughout the experiment (from $t = 0 \text{ s}$ to $t = 20 \text{ s}$); their color is the same of the sets of iso-displacement contours. Cold colors are for the smallest displacements and warm colors for the largest ones for both tracers and iso-displacement contours. The filled magenta disk (\bullet) is the last tracer to slip.

largest ones at Q_s . The outer contour defines the contact area at the instants (a) d_1 , (b) d_2 , and (c) d_s with the same color code as in the previous Figs. 3.1 and 3.3. The tracers lifted during the experiment are represented as filled disks, while open disks are for tracers present throughout the experiment; their color follows the same color code that

of the sets of iso-displacement contours, *i.e.* showing the magnitude of the tracers displacement. We assumed a displacement greater than 0.03 mm as a slip. This threshold (not equal to 0) is set to account for the unexpected displacement of the particles in the stuck regime due to their depth relative to the interface. Note that this fixed threshold should, ideally, be considered as a function of the PDMS bulk deformation under shear.

By following the evolution in time of the 0.03 iso-value curve, *i.e.* the limit between stuck and slip region, it can be seen that a micro-slip front moves inward from the contact periphery as shear increases. As expected, at $d = d_s$, this slip front converges and disappears around the last tracer to slip (show as a filled magenta disk in Fig. 3.8).

Both figures, Fig. 3.8 and Fig. 3.9, are consistent with a context of a partial slip, which is classical in sheared sphere/plane contacts, either rough [62] or smooth [61]. This scenario is also apparent in the movies (M185, M054, M025, and M005) where a peripheral slip region gradually invades the contact, replacing a central stuck area. Those observations are less evident to be performed with small normal loads, due to the lower density of tracers in such normal loads, hindering a more conclusive analysis.

To draw attention to some specific points of Fig. 3.8, Fig. 3.10 shows, on the left axis, the displacement curves for the last tracer to slip (blue line), the first never lifting tracer to slip (red line), and the first lifted tracer to slip (black line) as a function of time; on the right axis (grey color), $Q(t)$ is shown. The slope of the hatched area represents the velocity of the moving glass ($V = 0.1$ mm/s). Highlighting the evolution of those three tracers allows us to identify different stages during their evolution:

Stuck state (1-2): from the beginning of the displacement (1) when the glass plate starts to move, the tracers are dragged with the glass (no relative tracers displacement), up to the instant that the first tracer slips (2). Note that the first tracer to slip (black line) belongs to the set of tracers that will be lifted (in the four normal loads).

Partial slip (2-4): the slip of the first tracer (2) means that local slip occurs very soon after the onset of the shear. During the branch (2-4) more and more tracers start to slip at different instants as a slip front propagates inward (as can be seen in Fig. 3.9). This slip front defines the frontier between a slip and a stick region, meaning that during all this period the interface is under partial slip condition. At the instant (3) the first never lifted point starts to slip, and in (4) the last tracer slips and the macroscopic sliding regime initiates. This moment corresponds with the tangential force peak Q_s , at least

for the highest explored normal load. At lower loads, the lack of resolution of our set of experiment does not allow such a conclusion with high certainty. Note that the last tracer to slip is located in a central region on the contact area (filled magenta disk in Fig 3.9). The fact that the tracers start to slip at different instants results in a heterogeneous slip field, thus leading to the in-plane deformations discussed previously in Section 3.3.1.

Transient sliding (4-5): at the very beginning of sliding of each tracer, the slope of the curves seem to increase, meaning that the velocity of each tracer accelerates reaching a velocity even greater than the glass velocity V , *i.e.* the slope of the curves greater than the slope of the hatched area, before stabilising at V . Such transient sliding may be due to a process of interfacial relaxation, and its duration increases with the increase of the normal load, from (d) to (a) in Fig. 3.10. Note that for $P = 1.85\text{ N}$, the experiment duration was not sufficient to allow all tracers to stabilize their velocity at V .

Steady state sliding (5-end): after the accelerated sliding period, all slipping tracers reach the same velocity as the glass (5), *i.e.* the slopes of the curves and of the hatched area are the same, meaning that a steady macroscopic sliding is reached.

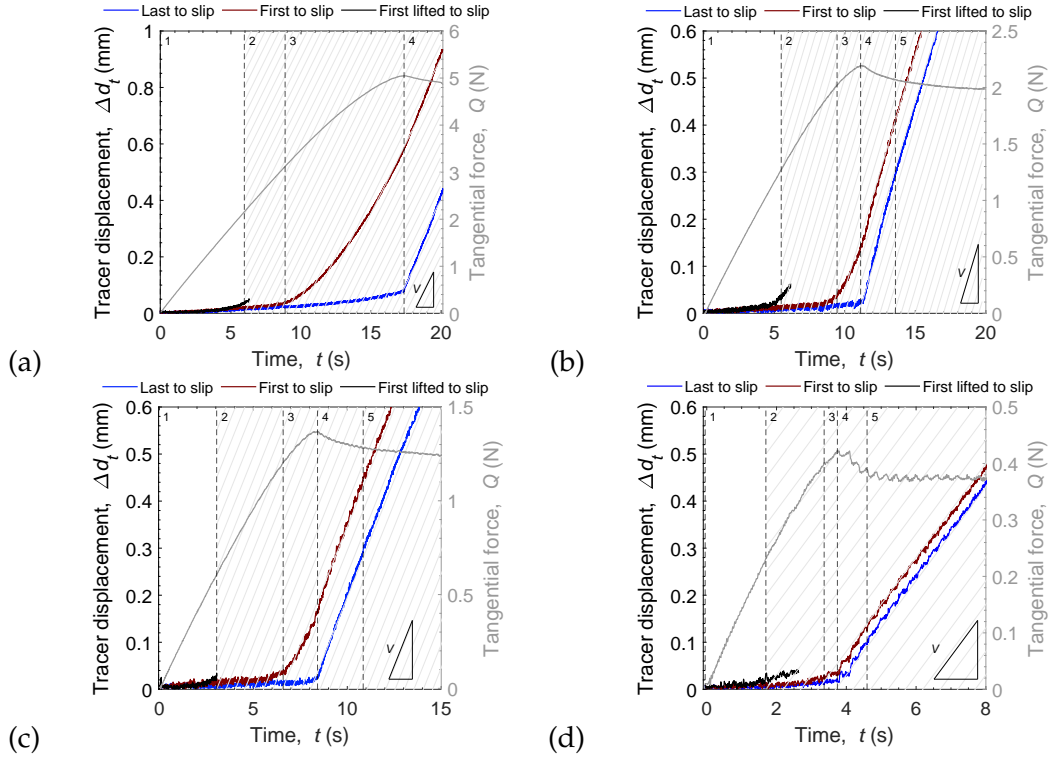


Figure 3.10: Evolution of the tracers for (a) $P = 1.85 \text{ N}$, (b) $P = 0.54 \text{ N}$, (c) $P = 0.25 \text{ N}$, and (d) $P = 0.05 \text{ N}$. Left axis (black color) is shown the last tracer to slip (blue line), the first never lifted tracer to slip (red line), and the first lifted tracer to slip (black line) as a function of the time; the right axis (grey color) shows $Q(t)$. Evolution states of the tracers: (1-2) stuck state, (2-4) partial slip, (3) first never lifted tracer to slip, (4-5) transient sliding, and (5) steady state sliding. The slope of the hatched area represents the velocity of the glass $V = 0.1 \text{ mm/s}$.

3.3.3 Finite-strain modelling of shear-induced contact area reduction

In collaboration with J. Lengiewicz and S. Stupkiewicz from Institute of Fundamental Technological Research (IPPT), Polish Academy of Sciences, a 3D model that combines a hyperelastic bulk and a non-adhesive but frictional interface was developed to evaluate the findings of the experimental analysis in terms of elementary mechanisms of shear-induced contact area reduction - lifting, laying, and in-plane deformation. The model results were prepared to be matched quantitatively with the literature experiments of [17, 63]. However, those literature results are similar enough to the ones obtained earlier in this chapter to enable a qualitative comparison with the same model. The results were presented in the published article “Finite deformations govern the anisotropic shear-induced area reduction of soft elastic contacts” [60], and a summary of the model and simulation part will be presented here.

Computational model: finite-strain framework and Tresca friction

The finite strain framework and Tresca friction model (see below) without adhesion are the two basic features of the model. They are combined with a finite element method as a suitable spatial discretization scheme. The contact problem under consideration, sketched in Fig. 3.11 from Lengiewicz et al. [60], corresponds to normal, and then tangential loading of a hyperelastic spherical solid in (adhesionless) frictional unilateral contact with a rigid plate.

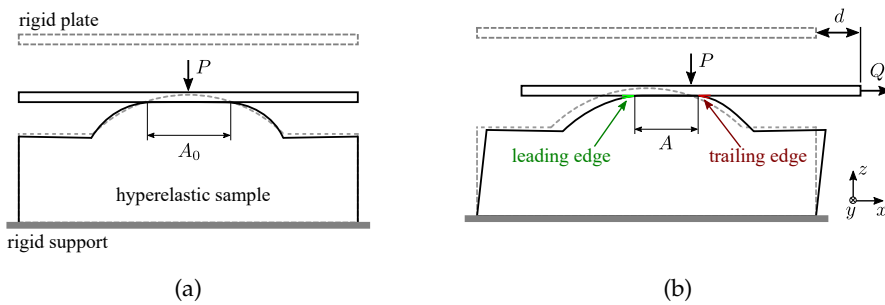


Figure 3.11: 2D sketch of the (3D) soft-sphere/rigid-plane contact under study. The initial (dashed lines) and deformed (solid lines) configurations are shown for two stages: (a) under pure normal load P and (b) when an additional tangential displacement d is applied, giving rise to a tangential load Q . In all subsequent figures, the leading (resp. trailing) edge is always on the left (resp. right) side. A_0 and A indicate the contact areas in the initial and deformed configurations, respectively. Figure from [60].

Hyperelasticity is treated using the nearly-incompressible isotropic neo-Hookean model. Such a model is used for predicting the nonlinear stress-strain behavior of materials, like elastomers and polymers, undergoing large deformations [84]. For the frictional behaviour of the contact interface, the Tresca model is employed. In this model, no local slip occurs until the contact shear strength σ is reached, and σ is assumed constant and independent on the normal contact traction. It was chosen because it is the simplest model that produces a proportional relation between the friction force of sphere/plane contact interface and its contact area, a relationship reported experimentally in many frictional contacts (see, e.g., Sahli et al. [17] and references therein). In the Tresca model, the proportionality constant will simply be the contact shear strength, σ .

The model parameters were taken to match their experimental counterpart in [17, 63]. The elastic properties of the elastomer sample are specified by the shear modulus μ and bulk modulus κ . Assuming a nearly incompressible response with the Poisson's ratio of $\nu = 0.49$, the Young's modulus has been identified as $E = 1.80 \text{ MPa}$. The

relationship between the parameters (E, ν) and (μ, κ) is given by $\mu = E / (2(1 + \nu))$ and $\kappa = E / (3(1 - \nu))$ and corresponds to a shear modulus of $\mu = 0.60 \text{ MPa}$ and a bulk modulus of $\kappa = 0.40 \text{ MPa}$. A value of $\mu = 0.60 \text{ MPa}$ was derived in a unique manner using the experimental values of P and $A(Q = 0)$. Similarly, a value of $\sigma = 0.41 \text{ MPa}$ was derived using the experimental values of A_s and Q_s . Note that the ratio σ/μ is significant, such that shear strains exceeding 50 % are expected. This is far beyond the range of validity of the small-strain theory, and of linear elasticity in particular, so that the finite-strain framework used in this study is, actually, essential. At those large strains, the mechanical behaviour of the elastomer used in the experiments of Sahli et al. [17, 63] (Sylgard 184) is already well beyond its linear range [85, 86].

Shear-induced contact area reduction

Firstly, using the computational model described above, the shear-induced contact area reduction in the literature sphere/plane experiments of Sahli et al. [17, 63] were simulated and qualitatively compared in Fig 3.12. Fig. 3.12(a) directly compares the predicted $A(Q)$ curves with those of Sahli et al. [17] (see their Fig. 2C). The solid red line correspond to the relation $Q = \sigma A$. Figure 3.12(b) compares the predicted contact sizes along and orthogonal to shear, ℓ_{\parallel} and ℓ_{\perp} respectively, with those of Sahli et al. [63] (see their Fig. 3b). In both cases, the amplitudes and shapes of the curves are well captured, although the model slightly underestimates A and does not capture the slight increase of ℓ_{\perp} observed in the experiments.

Elementary mechanisms of contact area reduction

Secondly, a thorough analysis of the simulation results of this model was used to validate the experimental findings of Section 3.3.1, to test whether the elementary mechanisms - lifting, laying and in-plane deformation - responsible for contact area reduction in the experiment can also be identified in the model.

Figure 3.13 shows the evolution of the contact area, for the normal loads $P = 0.27 \text{ N}$ and $P = 2.12 \text{ N}$, during the incipient tangential loading at five selected displacements of the rigid plate: $d_0 = 0$, d_s at the onset of global sliding and three intermediate configurations (d_i). The nodes of the elastic surface are labeled in red if they have undergone some local slip, in blue if they are still stuck to the same point of the rigid plate, and

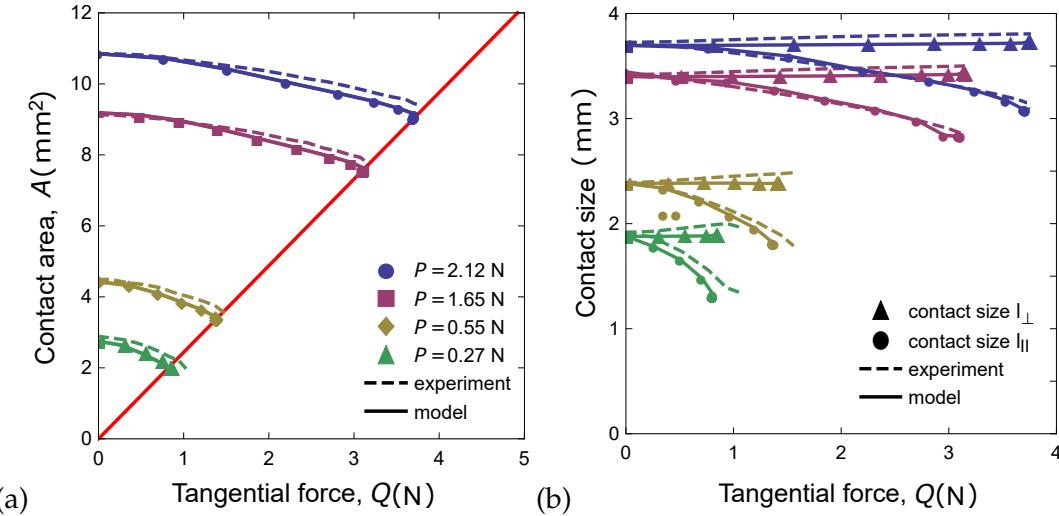


Figure 3.12: Comparison of the model predictions obtained for the model, for all normal loads, to the experimental results of [17, 63]. (a) A vs Q . Solid straight red line: $Q = \sigma A$. (b) Contact size along (ℓ_{\parallel}) and perpendicular to (ℓ_{\perp}) the shear loading direction vs Q . Figure adapted from [60].

in green if they were initially in contact and not anymore at the onset of macroscopic sliding.

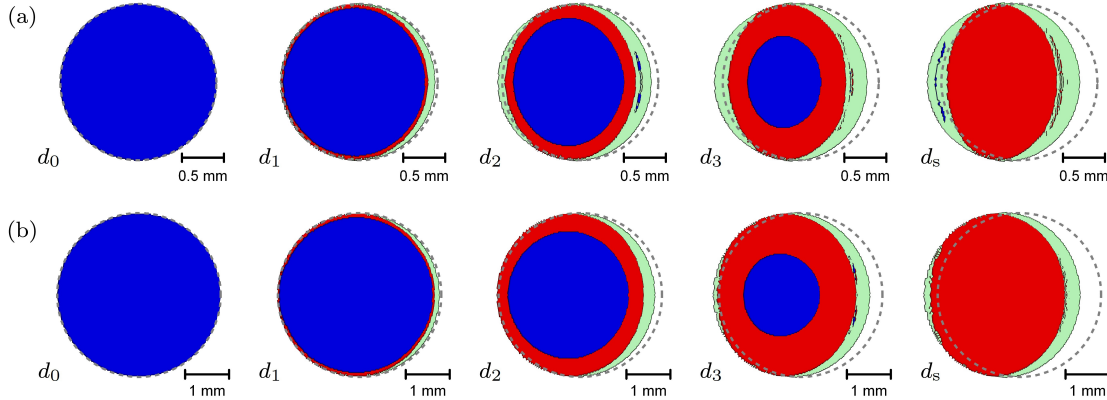


Figure 3.13: Evolution of the contact zones for (a) $P = 0.27$ N (d_1, d_2, d_3 : 35, 61, 81 % of $d_s = 0.45$ mm) and (b) $P = 2.12$ N (d_1, d_2, d_3 : 29, 58, 80 % of $d_s = 1.04$ mm) shown in the frame attached to the moving rigid plate. Dashed circles indicate the boundary of the initial contact zone (at d_0). Blue and red regions denote the stick and slip zones, respectively. Green regions indicate the current (deformed) location of the initial contact zone that has been lifted. The leading edge is on the left. Figure from [60].

As in the experimental findings observed earlier in this chapter and in the experiments of Sahli et al. [63], the contact zone and the stick zone have an elliptical shape, the related shear-induced anisotropy increases with increasing displacement d and is higher for the lower normal loads.

The labeled nodes allow us to identify the same mechanism as those found in the experiments. First, the region of contact lifting clearly corresponds to the green region

around the final contact zone, *i.e.* the region that corresponds to nodes that have been lifted out-of-contact during the incipient loading due to the shear-induced deformations of the elastic sphere. Second, region of contact laying correspond to small parts (hardly visible in Fig. 3.13 d_s) of the final contact which are found outside the deformed initial contact region (shown as a green region in the current configuration). These nodes were initially out of contact, but laid into contact during the incipient tangential loading. Finally, in-plane deformation, related to inhomogeneous slip, is also find in the model within the contact zone and leads to either “in-plane compression” or “in-plane dilation”. Indeed, in Fig. 3.13, the slip zone advances from the contact periphery towards the centre at the expense of the stick zone until the stick zone vanishes and full sliding occurs. As in our experiments (see Fig. 3.9), an inward slip front, corresponding to the boundary of the blue region (*i.e.* the frontier between the stick and slip zones) can be identified and is responsible for the inhomogeneous strain field at the interface. Such deformations extend beyond the contact region, which explains why the boundary of the green zone does not coincide with the dashed circle.

The partial slip configurations, as those seen in Fig. 3.13, are classically found (with a circular stick zone) in models of sheared frictional linear elastic sphere/plane contact [30, 83]. They typically correspond to heterogeneous slip fields, thus causing in-plane deformations.

Figure 3.14 provides a detailed insight into this last mechanism, by showing the field of local surface dilation/compression. For each contact node i , its tributary area (*i.e.* the area associated with the node) is computed both in the initial configuration (at d_0), A_0^i , and in the current configuration, A^i . The color map in Fig. 3.14 corresponds to the local surface dilation/compression, $(A^i - A_0^i)/A_0^i$. Surface dilation is observed close to the leading edge while compression is observed close to the trailing edge. The decreasing green elliptical region in the middle of the contact zone, in which the local surface dilation/compression is equal to zero, corresponds to the stick zone in Fig. 3.13.

Figure 3.15 compares the individual contributions of all mechanisms to the total relative contact area change in the model. For all normal loads, the model predicts that lifting represents about 90–95 % of the total shear-induced area reduction, indicating it as the primary mechanism responsible for the area reduction. The contributions of dilation and compression are individually significant, however, they essentially cancel

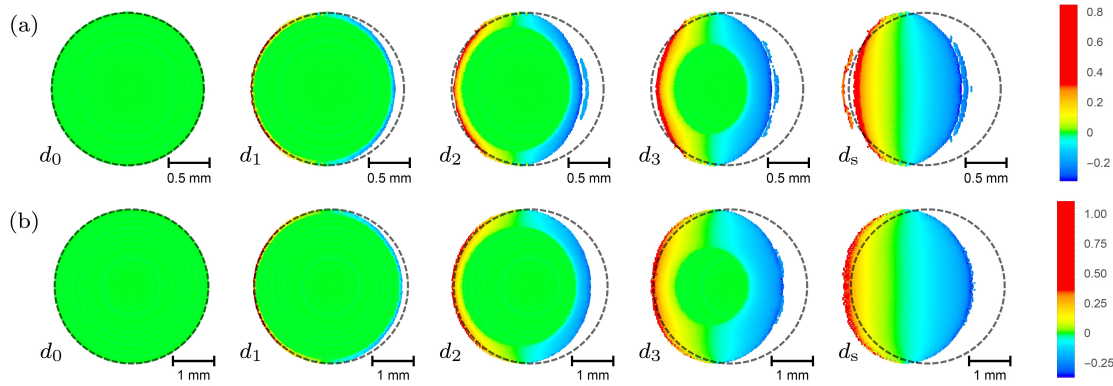


Figure 3.14: Evolution of the field of surface dilation/compression, $(A^i - A_0^i)/A_0^i$, shown in the frame attached to the moving rigid plate for (a) $P = 0.27 \text{ N}$ and (b) $P = 2.12 \text{ N}$, and for the same select displacements as in Fig. 3.13. Dashed circles indicate the boundary of the initial contact zone. The leading edge is on the left. Figure from [60].

each other out, so that the in-plane deformation is responsible only for about 5–10 % of the total area reduction. Contact laying is rarely observed (if so, at the leading edge only), therefore its contribution to the total area reduction is essentially negligible in the model.

We emphasize that the relevant lifting in our model is a local lifting due to shear deformations of the elastic sample, rather than a shear-induced global lifting of the rigid plate. Such a global lifting, although existing in the constant normal load setting of the model, has been found to be only about 4 % of the normal displacement associated with the initial, purely normal loading. Thus, it is far from sufficient to explain the 15–30 % area reduction observed in Fig. 3.15.

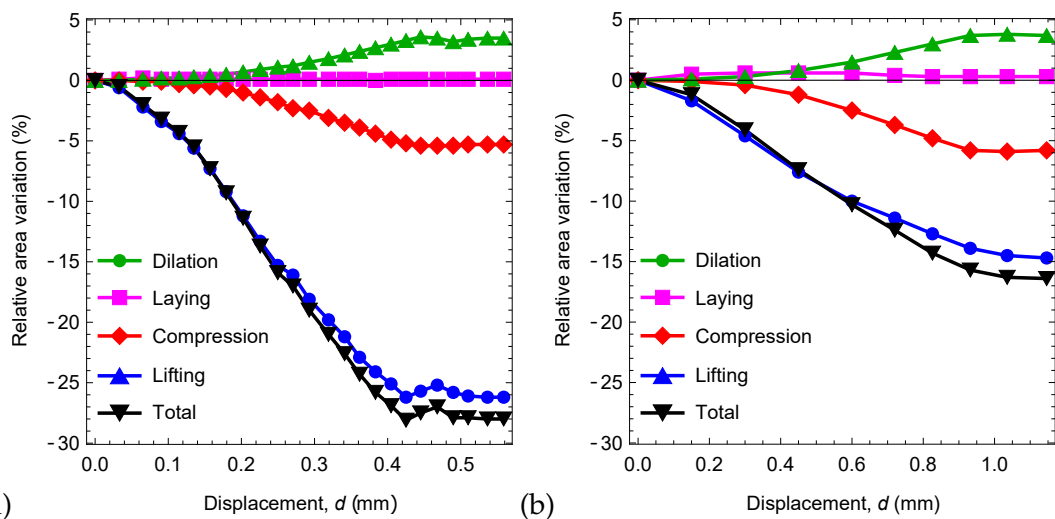


Figure 3.15: Evolution of the individual contributions of the various elementary mechanisms to the total relative area variation $\Delta A/A_0$ as a function of the rigid plate displacement d . (a) $P = 0.27 \text{ N}$ and (b) $P = 2.12 \text{ N}$. Figure adapted from [60].

Summary

The model just presented has been shown to capture quantitatively the experimental results of [17, 63] about the anisotropic shear-induced area reduction of sphere/plane elastomer contacts for relatively large normal loads (Fig. 3.12) and also the results of the experimental observations presented in this chapter. The agreement was obtained without any adjustable parameter, in the sense that virtually all model parameters are set by independent measurements on the same experimental system. Those parameters are: the geometry of the hyperelastic neo-Hookean sample, its shear modulus, and the contact shear strength of the PDMS/glass interface. This absence of adjustable parameters provides the presented model with a decisive comparative advantage over competing models with reduced contact area induced by shear. Especially, fracture-like adhesion-based models, that in order to offer a good quantitative agreement with experiments [53, 87], require a prescription of finely-tuned mode-mixity functions [52]. The presented 3D model also captures the anisotropic evolution of the contact shape, whereas most fracture-based adhesive models assume axisymmetry of the contact (see Papangelo et al. [53] for the only exception, to our knowledge).

The direct implication of the model is that finite-deformation effects and the non-linear elasticity of elastomers are presumably the key ingredients explaining the experimental results, rather than viscoelasticity or adhesion. Nevertheless, the model has only been applied to contacts submitted to relatively large normal load, in the newton range [17], while other experiments have used much smaller normal loads, in the millinewton range [46, 49, 55]. For those smaller loads, adhesive stresses may be of the order of, or even exceed, contact stresses, and non-linear elasticity may be not the only dominant ingredient for shear-induced contact shrinking anymore. Identifying the normal load regimes in which adhesion needs to be accounted for is an important goal not only for future contact mechanics models but also for experiments. In face of this, we will present in Chapter 4 an experimental study in a wide range of normal loads.

3.4 Discussion

An original experimental analysis using an elastomer sphere seeded with particles identified different stages during the sliding process and the presence of three elementary mechanisms - lifting, laying, and in-plane deformation - responsible for the anisotropic contact area reduction. Although a higher area density of tracers would be desirable to reduce the measurement uncertainties, particularly at small loads (Section 3.3.1), lifting is presumably the dominant area reduction mechanism, while a non negligible contribution of the laying and in-plane mechanisms exists as the normal load increases. The observations suggest that the contributions of those mechanisms are load-dependent and that different phenomena govern at small and large normal loads.

A typical transition between a stuck state to a sliding one, *i.e.* the transition between the static to kinetic friction is usually defined by a peak in a tangential-time curve followed by an abrupt decrease. However, experimentally, such a peak is not well apparent, which leads us to question: *where is the onset of sliding?* The observations in Section 3.3.2 show that the frictional sliding undergoes different stages and partial slip starts well below the static friction force Q_s with micro slip occurring at different instants, for different tracers, until Q_s . The profile of tracers' trajectory has shown a quite asymmetrical displacement in the contact zone and a less pronounced transition to macroscopic sliding as the normal load increases. Surprisingly, the velocity of the tracers reached a velocity even greater than the glass velocity V before finally reaching it. As pointed out, such observation may be due to a process of interfacial relaxation, that is, the interface is in a deformed state, it has stored elastic energy, and part of this elastic energy must be restored to return to a less-deformed state during the macroscopic sliding state.

The incipient shear-loading of smooth sphere/plane elastic contacts is characterized in the experiments and in the model by two propagating fronts: a lifting front at the contact periphery, and a non-circular micro-slip front within the contact area. The existence of those two different fronts, although explicitly acknowledged by some authors [58, 88], has never been properly described in fracture-based adhesive models. Indeed, in those models, the additional energy dissipation in the contact due to frictional micro-slip, and described via the mode-mixity function, is assumed to be located

at the contact periphery, and not within a growing, finite region of the contact.

For the first time, the elementary mechanisms of area change were quantified. And, as in the experiments, the modeling results suggest that for the experimental conditions used in [17, 63], local lifting is the main mechanism explaining the significant area reduction observed and its anisotropy (Fig. 3.15). For all normal loads explored, this conclusion is true, with the total area reduction being dependent on the normal load (as also observed experimentally).

In summary, lifting is presumably the main area reduction mechanism in both experiments and model. While experiments revealed a potentially larger contribution of the laying and in-plane mechanisms for large normal loads, a definitive quantitative comparison with the model is hindered by the finite experimental resolution. Also note that, due to the higher contact shear strength (0.53 rather than 0.41 MPa) and smaller Young's modulus (1.5 rather than 1.8 MPa) of this chapter's experiments compared to those of [17, 63], the numerical model could not converge in those more severe conditions, thus impeding direct comparison between model and tracer-based experiments. Such a comparison is also an important challenge for future work.

Finally, the simplicity and generality of the model assumptions suggest that the results may be also relevant to other systems than the elastomer sphere/plane contacts studied here. First, non-linear elasticity being a generic feature of soft materials, from gels to human skin, we expect it to be a likely mechanism for contact area reduction in all studies involving such materials. It would thus be interesting to re-interpret recent experiments like those of e.g. [87] on polyacrylonitrile or those of [17, 89] on human fingertips, from the standpoint of finite-deformation mechanics. Second, [17, 63] argued that the mechanisms of shear-induced anisotropic contact area reduction may be the same in millimetric sphere/plane contacts and in individual micrometric junctions within rough contact interfaces. Such a similarity across scales suggests that the present conclusions may also be used to further understand the shear behaviour of soft material multicontacts, the modelling of which may require non-linear elasticity. This may in particular be an explanation for the fact that, in [90], a multi-asperity model based on linear elasticity failed to reproduce quantitatively the multicontact results of [17].

3.5 Conclusion

An original experimental analysis was proposed to show the existence of elementary mechanisms responsible for the evolution of the contact area under shear. First, it was demonstrated that contact lifting and contact laying do occur and can be quantified using Voronoi tessellation. Second, using Delaunay triangulation, the progressive development of a heterogeneous in-plane strain field within the contact area was illustrated. The existence of those mechanisms seems to be normal load-dependent. Under large load, contact lifting and contact laying occur on opposite sides of the periphery of the contact area, while under small load, contact lifting occurs at both sides. The challenges associated with the experimental approach has been thoroughly discussed.

With the tracking of the particles we could measure their displacement relative to its initial position in the contact area and identify a micro-slip front that moves from the contact periphery inward the contact region as shear increases, replacing a central stuck area. We highlighted different stages during their evolution: a stuck state, a partial slip, a transient sliding, and steady state sliding.

The findings, under large load, were qualitatively compared with a developed model proposing for the first time a non-adhesive, non-viscous model of shear-induced contact area reduction in soft materials. Quantitative agreement with the recent experimental results of Sahli et al. [17, 63] on sphere/plane elastomer contacts has been obtained, with no adjustable parameter, using the Tresca friction law and the neo-Hookean hyperelastic model. The necessary ingredients for this agreement are finite deformations and non-linear elasticity.

All results suggest a new perspective on the phenomenon of shear-induced contact area reduction in soft materials. This currently highly debated topic has been dominated by interpretations based on a leading role of adhesion. Here, instead, it was suggested that finite-deformation effects and non-linear elasticity can be equally important, all the more so as large normal loads are considered. Clarification of the validity domains where adhesion and/or finite deformations need to be accounted for remains a major open issue on the topic.